Ultrastrong coupling between electron tunneling and mechanical motion

Florian Vigneau [1,*] Juliette Monsel [2,*] Jorge Tabanera [3] Kushagra Aggarwal [1] Léa Bresque [4] Federico Fedele [1]
Federico Cerisola,[1,5] G. A. D. Briggs [1] Janet Anders,[5,6] Juan M. R. Parrondo [3] Alexia Auffèves,[4] and Natalia Ares [1,7]

[1]*Department of Materials, University of Oxford, Oxford OX1 3PH, United Kingdom*

[2]*Department of Microtechnology and Nanoscience (MC2), Chalmers University of Technology,
S-412 96 Göteborg, Sweden*

[3]*Department of Structure of Matter, Thermal Physics and Electrodynamics and GISC,
Universidad Complutense de Madrid, Pl. de las Ciencias 1, 28040 Madrid, Spain*

[4]*Univ. Grenoble Alpes, CNRS, Grenoble INP, Institut Néel, 38000 Grenoble, France*

[5]*Physics and Astronomy, University of Exeter, Exeter EX4 4QL, United Kingdom*

[6]*Institut für Physik, Potsdam University, 14476 Potsdam, Germany*

[7]*Department of Engineering Science, University of Oxford, Oxford OX1 3PJ, United Kingdom*

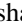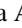The ultrastrong coupling of single-electron tunneling and nanomechanical motion opens exciting opportunities to explore fundamental questions and develop new platforms for quantum technologies. We have measured and modeled this electromechanical coupling in a fully suspended carbon nanotube device and report a ratio of $g_m/\omega_m = 2.72 \pm 0.14$, where $g_m/2\pi = 0.80 \pm 0.04$ GHz is the coupling strength and $\omega_m/2\pi = 294.5$ MHz is the mechanical resonance frequency. This is well within the ultrastrong coupling regime and the highest among all other electromechanical platforms. We show that, although this regime was present in similar fully suspended carbon nanotube devices, it went unnoticed. Even higher ratios could be achieved with improvement on device design.

I. INTRODUCTION

Ultrastrong coupling between a quantum system and a nanomechanical resonator is reached when the ratio between the coupling strength g_m and the mechanical resonance frequency $\omega_m/2\pi$ is greater than one. In the dispersive regime, such high coupling opens a wide range of possibilities for the development of promising applications in quantum information processing [1], high-precision sensors [2–4], cooling [5], transfer of quantum states to mechanical motion [6,7], and in the exploration of the foundation of quantum mechanics [8]. The main reason for these promising features lies in the strong back action of a single photon or electron on the mechanical motion. Unprecedented control over quantum states is then available and macroscopic quantum states can be created allowing for foundational tests of quantum mechanics. Recent proposals suggest that work extraction at the nanoscale is possible in the ultrastrong coupling regime [9,10], as well as the study of fluctuation theorems [10] and study of systems far from equilibrium [11,12].

Among the large variety of optomechanical and electromechanical platforms developed [13–23], the ultrastrong coupling between quantum states and mechanical motion

is within reach only for a few, including superconducting circuits ($g_m/\omega_m \simeq 0.35$) [24], NV centers embedded in semiconducting nanowires under a magnetic field gradient ($g_m/\omega_m \simeq 0.1$) [25], and quantum dots in semiconducting
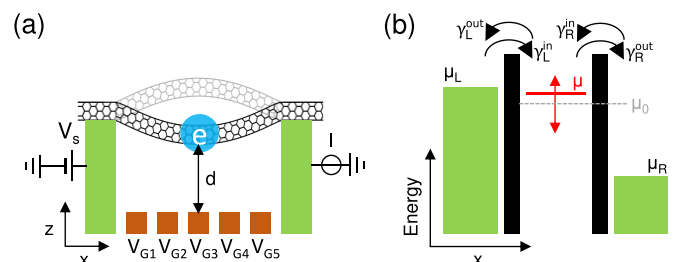
FIG. 1. (a) Schematic of the device. A carbon nanotube is suspended between two metallic reservoirs and over an array of gate electrodes to which we apply gate voltages V_{G1-G5}. A bias voltage V_s drives a current I through the nanotube, within which a quantum dot is electrostatically defined. The single-electron tunneling through the quantum dot couples to the nanotube's motion. The coupling strength depends on the distance d between the quantum dot and the gate electrodes. (b) Schematic diagram of the electrochemical potential levels of a quantum dot. The left (L) and right (R) tunnel rates from the reservoirs to the quantum dot are indicated γ_L^{in}, γ_L^{out}, γ_R^{in} and γ_R^{out}. The electrochemical potentials of left and right contacts are μ_L and μ_R, respectively, and their energy difference defines a bias window. When the carbon nanotube vibrates, the electrochemical potential of the quantum dot μ shifts with respect to a reference electrochemical potential μ_0, which is controlled by the gate electrodes. The red arrow symbolizes the change in μ caused by the nanotube's motion.

---

nanowires, for which strain is the coupling mechanism ($g_\mathrm{m}/\omega_\mathrm{m} \simeq 0.85$) [26,27]. Theoretical proposals indicate that the ultrastrong coupling could be reached in SQUIDs with a mechanical compliant segment [28–31], single atoms in a cavity [32,33], or Cooper pair boxes [34–36].

Quantum dots electrostatically defined in fully suspended carbon nanotube devices [Fig. 1(a)] offer a high degree of control over the confinement potential [37]. The mechanical properties of carbon nanotubes are also exceptional; comparatively large zero-point motion, quality factors as high as 5×10^6 [38], and mechanical frequencies up to 39 GHz [39].

When the carbon nanotube is in motion, its displacement changes the distance between the carbon nanotube and the gate electrodes. The quantum dot is thus capacitively coupled to the nanotube's motion. The first evidence of this effect was the observation that single-electron tunneling creates periodic modulations of the mechanical resonance frequency [22,23,37,40–42]. These modulations of the mechanical resonance frequency, also called softening, are a signature of the electromechanical coupling between charge states and mechanical motion [43,44]. This coupling allowed for the realization of coherent mechanical oscillators driven by single-electron tunneling [45], cooling of the mechanical motion [46], and probing of electronic tunnel rates [47]. Fully suspended carbon nanotube devices in the ultrastrong coupling regime have been proposed for the realization of nanomechanical qubits [48]. A recent study has demonstrated so-called deep-strong coupling [49], which is the equivalent of ultrastrong coupling between a carbon nanotube quantum dot and a THz resonator [50]. Until now, a careful experimental estimation of the electromechanical coupling strength that carbon nanotube devices can offer was still missing.

In this work we show that the electromechanical coupling in fully suspended carbon nanotube devices can reach the ultrastrong coupling regime and that it presents one of the highest coupling ratios reported so far; $g_\mathrm{m}/\omega_\mathrm{m} \simeq 2.72$. We obtain this ratio using two independent approaches. We measure the periodic modulations of the mechanical resonance frequency resulting from single-electron tunneling in our experiment and model it using a rate equation model. We also simulate the quantum dot energy levels as the carbon nanotube position changes in the plane of motion. Both approaches lead to similar conclusions and converge to the same quantitative value of g_m. The observed coupling ratios can be improved further by adapting the geometry of the device.

II. SYSTEM AND ELECTROMECHANICAL MODEL

We focus on a carbon nanotube device with a suspended segment of approximately 800 nm [see Fig. 1(a)]. The quantum dot is defined in the nanotube through a combination of Schottky barriers at the contacts and the voltages applied to five gate electrodes (labeled V_{G1-G5}) beneath the nanotube. These gate electrodes are also used to actuate the nanotube's motion [45,51,52]. A current I is driven by a bias voltage V_s. All experiments are performed at 40 mK.

To model the interplay between the single-electron transport through the quantum dot and the nanotube's mechanical motion in this device, we use rate equations. First, we describe the electron transport through the device. Applying a bias voltage V_s between the source (left) and drain (right) reservoirs opens up an energy window $eV_\mathrm{s} = \mu_\mathrm{L} - \mu_\mathrm{R}$, where e is the charge of an electron, and μ_L and μ_R are the electrochemical potentials of the left and right reservoirs, respectively. If within this energy window, which we will refer to as bias window, there is an electrochemical potential level μ corresponding to a transition that involves the charge state of the quantum dot, electrons can tunnel from one reservoir onto the quantum dot and off to the other reservoir.

We calculate the current I as a function of the quantum dot electrochemical potential μ. The quantum dot is weakly coupled to left and right reservoirs [see Fig. 1(b)], and this coupling is parameterized by four effective tunnel rates; tunneling from the left/right reservoir to the quantum dot [$\gamma_\mathrm{L/R}^\mathrm{in}(\mu)$] and tunneling from the quantum dot to the left/right reservoir [$\gamma_\mathrm{L/R}^\mathrm{out}(\mu)$] [42]. These effective tunnel rates correspond to the product of the left/right tunnel barrier rates [$\Gamma_\mathrm{L/R}$] and the overlap between the density of states of the quantum dot and left/right reservoirs, $\rho_\mathrm{L/R}(\mu)$, i.e.

$$\gamma_\mathrm{L/R}^\mathrm{in}(\mu) = \Gamma_\mathrm{L/R}\, \rho_\mathrm{L/R}(\mu), \tag{1a}$$

$$\gamma_\mathrm{L/R}^\mathrm{out}(\mu) = \Gamma_\mathrm{L/R}(1 - \rho_\mathrm{L/R}(\mu)). \tag{1b}$$

The tunneling through the quantum dot occurs at a rate $\Gamma_\mathrm{tot} = \sum_{\mu=L,R}(\gamma_\mu^\mathrm{in} + \gamma_\mu^\mathrm{out}) = \Gamma_\mathrm{L} + \Gamma_\mathrm{R}$. As we will show later, $\Gamma_\mathrm{tot}/2\pi$ is of the order of 100 GHz, and thus $\hbar\Gamma_\mathrm{tot} \gg k_\mathrm{B}T$ for sub-Kelvin temperatures, with k_B the Boltzmann constant. In this regime, we find [42,53]

$$\rho_\mathrm{L/R}(\mu) = \frac{1}{2} + \frac{1}{\pi}\arctan\left(\frac{2(\mu_\mathrm{L/R} - \mu)}{\hbar\Gamma_\mathrm{tot}}\right). \tag{2}$$

We can thus express the current flowing through the quantum dot as

$$I(\mu) = e\,\frac{\gamma_\mathrm{L}^\mathrm{in}(\mu)\gamma_\mathrm{R}^\mathrm{out}(\mu) - \gamma_\mathrm{R}^\mathrm{in}(\mu)\gamma_\mathrm{L}^\mathrm{out}(\mu)}{\Gamma_\mathrm{tot}}. \tag{3}$$

We now examine how the mechanical motion affects the electron transport. As the carbon nanotube moves, its displacement z in the vertical direction changes the capacitance between the gate electrodes and the quantum dot. This leads to a change in μ proportional to the electromechanical coupling constant g_m at the first order in the displacement (see Appendix A),

$$\mu(z) \simeq \mu_0 + \hbar g_\mathrm{m}\frac{z}{z_\mathrm{ZPM}}, \tag{4}$$

where $z_\mathrm{ZPM} = \sqrt{\hbar/2m\omega_\mathrm{m}}$ is the zero-point motion, with m the nanotube's mass (see Appendix B 4 for details on the estimation of the carbon nanotube's mass), and μ_0 is the electrochemical potential of the quantum dot for a carbon nanotube displacement equal to 0, i.e., at $z = 0$. We can control μ_0 with the applied gate voltages.

The change in μ caused by the nanotube's motion produces a change in the average population of the quantum dot. This change can be considered adiabatic if $\Gamma_\mathrm{tot} \gg \omega_\mathrm{m}$. This means

that, on the timescales corresponding to the mechanical motion, the average population instantaneously reaches a steady state and is purely defined by the position of the carbon nanotube. In this regime, electron-vibron coupling mechanisms such as the Franck-Condon blockade [54–56] are negligible. In this case, we find that the relative average occupation of the quantum dot with reference to a fixed charge state is

$$p(\mu(z)) = \frac{\gamma_{\mathrm{L}}^{\mathrm{in}}(\mu(z)) + \gamma_{\mathrm{R}}^{\mathrm{in}}(\mu(z))}{\Gamma_{\mathrm{tot}}}. \tag{5}$$

Note that p is a number between 0 and 1.

The mechanical motion is in turn affected by the electron transport. Variations of p cause the reduction of the mechanical resonance frequency that is considered a signature of strong electromechanical coupling in nanotube mechanical resonators [22,23,37,40–42]. The effective resonance frequency $\omega_{\mathrm{m}}^{\mathrm{eff}}(\mu_0)/2\pi$, lower than $\omega_{\mathrm{m}}/2\pi$, is observed when μ varies within the bias window $[\mu_{\mathrm{R}}, \mu_{\mathrm{L}}]$. This interplay between single-electron transport and mechanical motion can be explored further by writing the equation of motion that models the carbon nanotube displacement (see Appendix A),

$$\ddot{z} + \omega_{\mathrm{m}}^2 \left[z + 2p(\mu(z)) \frac{g_{\mathrm{m}}}{\omega_{\mathrm{m}}} z_{\mathrm{ZPM}} \right] = 0. \tag{6}$$

Since carbon nanotube devices exhibit high-quality factors, we neglect the mechanical damping over a few mechanical periods.

The combination of Eqs. (5) and (6) makes explicit that p can change within a mechanical oscillation, since p depends on μ, and μ depends on z [Eq. (4)], which is a function of time. Considering that μ has a weak dependence on z, the rest position of the resonator $z_r(p) = -2p(\mu)(g_{\mathrm{m}}/\omega_{\mathrm{m}})z_{\mathrm{ZPM}}$, is obtained for $\ddot{z} = 0$. Figures 2(a)–2(c) show the nanotube's displacement z and dot population p as a function of time, as well as the corresponding trajectories in phase space, obtained by solving Eq. (6) numerically for different values of μ_0. When μ_0 is far above the bias window ($\mu_0 \gg \mu_{\mathrm{L}}$), $p(\mu) = 0$ and the resonator rest position is $z_r(0) = 0$ (dash-dotted green line). Conversely, when μ_0 is far below the bias window ($\mu_0 \ll \mu_{\mathrm{R}}$), the population is $p(\mu) = 1$ and the nanotube's rest position is $z_r(1) = -2(g_{\mathrm{m}}/\omega_{\mathrm{m}})z_{\mathrm{ZPM}}$ (dashed blue line). But when μ_0 is within the bias window, $p(\mu)$ varies between 0 and 1, i.e. $0 \leqslant p(\mu) \leqslant 1$, and the nanotube's rest position satisfies $0 \geqslant z_r(p) \geqslant -2(g_{\mathrm{m}}/\omega_{\mathrm{m}})z_{\mathrm{ZPM}}$ (solid orange line). The nanotube's motion follows a trajectory in phase space at constant angular velocity ω_{m} but the rest position $(0, z_r(p))$ shifts with $p(t)$, making the trajectory elliptical instead of circular [see Fig. 2(b)]. As a result, when p is not constant (solid orange line), the period can exceed $2\pi/\omega_{\mathrm{m}}$, leading to a reduction of the effective mechanical resonance frequency $\omega_{\mathrm{m}}^{\mathrm{eff}}(\mu_0)/2\pi$, evident in Fig. 2(a).

Under the approximation of small displacements, the effective resonance frequency can be estimated from Eq. (6). Linearizing $p(\mu)$, we obtain

$$p(\mu) = p(\mu_0) + (\mu - \mu_0) \left. \frac{\partial p}{\partial \mu} \right|_{\mu_0}. \tag{7}$$
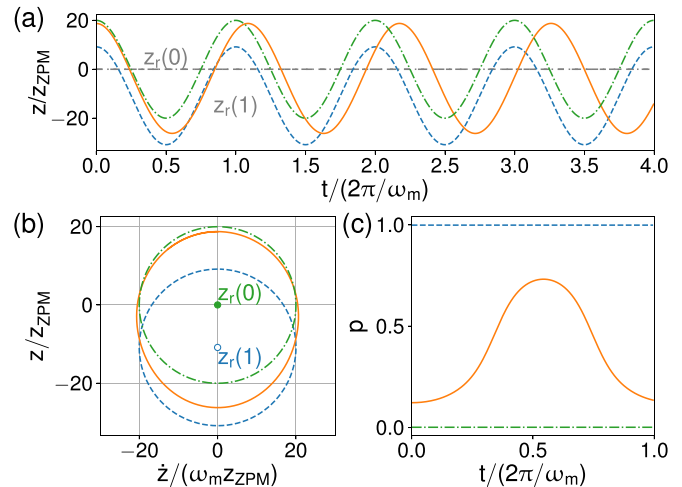

FIG. 2. Time evolution obtained by numerically integrating the equation of motion (6), starting from the initial conditions $z(0) = z_0 + z_r(p(\mu(z_0)))$ and $\dot{z}(0) = 0$, with $z_0/z_{\mathrm{ZPM}} = 20$, for three different values of μ_0: well above the bias window ($\mu_0 \gg \mu_{\mathrm{L}}$, dash-dotted green lines), within the bias window ($\mu_0 = 0$, solid orange lines), and well below the bias window ($\mu_0 \ll \mu_{\mathrm{R}}$, dashed blue lines). This choice of $z(0)$ results in identical amplitudes for the cases $\mu_0 \gg \mu_{\mathrm{L}}$ and $\mu_0 \ll \mu_{\mathrm{R}}$. (a) Nanotube's displacement z as a function of time over four mechanical periods. Gray lines indicate the nanotube's rest position for $p = 0$ and $p = 1$: $z_r(0) = 0$ and $z_r(1) = -2(g_{\mathrm{m}}/\omega_{\mathrm{m}})z_{\mathrm{ZPM}}$. (b) Corresponding phase space trajectories over one mechanical period. The dots indicate the resonator's rest position for $p = 0$ and $p = 1$: $z_r(0)$ (green point) and $z_r(1)$ (blue circle). (c) Population of the quantum dot as a function of time over one mechanical period. These simulations, use the parameters extracted from the experiment (see main text); $\omega_{\mathrm{m}}/2\pi = 294.5\,\mathrm{MHz}$, $\Gamma_{\mathrm{L}}/2\pi = 1.0\,\mathrm{GHz}$, $\Gamma_{\mathrm{R}}/2\pi = 40\,\mathrm{GHz}$, and $z_{\mathrm{ZPM}} = 0.68\,\mathrm{pm}$ (see Appendix B). In the plots, the value of $g_{\mathrm{m}}/2\pi$ was exaggerated by a factor 2 for visual clarity; $g_{\mathrm{m}}/2\pi = 1.6\,\mathrm{GHz}$ while the true value is 0.8 GHz.

We introduce this expression in Eq. (6) and use Eq. (4) to rewrite the equation of motion as follows:

$$\ddot{z} + \left[\omega_{\mathrm{m}}^2 + 2g_{\mathrm{m}}^2 \hbar \omega_{\mathrm{m}} \left. \frac{\partial p}{\partial \mu} \right|_{\mu_0} \right] z = -2p(\mu_0)g_{\mathrm{m}}\omega_{\mathrm{m}} z_{\mathrm{ZPM}}. \tag{8}$$

Thus the effective resonance frequency is

$$\omega_{\mathrm{m}}^{\mathrm{eff}}(\mu_0) = \sqrt{\omega_{\mathrm{m}}^2 + 2g_{\mathrm{m}}^2 \hbar \omega_{\mathrm{m}} \left. \frac{\partial p}{\partial \mu} \right|_{\mu_0}}. \tag{9}$$

Note that $\partial p/\partial \mu$ is negative.

III. EXPERIMENTAL RESULTS

To verify the validity of this prediction in our device and estimate the coupling strength g_{m}, we use gate voltages to define a single quantum dot, revealed by the Coulomb diamonds in Fig. 3(a). From this measurement, we estimate the lever arm $\alpha = 0.054^{+0.007}_{-0.005}\,\mathrm{eV/V}$ and its uncertainty (see Appendix B 2), which relates the variation of μ_0 with the applied gate voltages $\Delta\mu_0 = -\alpha\Delta V_{\mathrm{G1}}$. Measurements in Figs. 3(a), 3(b) were performed with the carbon nanotube at rest (no driven motion), and thus μ is equal to μ_0. From a fit of a Coulomb peak
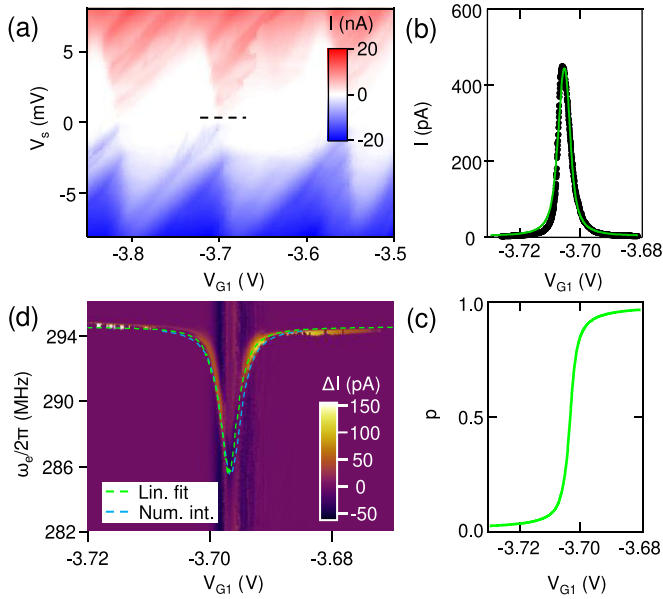
FIG. 3. (a) Current as a function of V_s and V_{G1} with $V_{G2} = 0\,\text{V}$, $V_{G3} = -4\,\text{V}$, $V_{G4} = 0\,\text{V}$, $V_{G5} = -3.95\,\text{V}$ and $R_s = 100\,\text{k}\Omega$. We observe Coulomb diamonds, evidencing single-electron tunneling. (b) Current as a function of V_{G1} for $V_s = 0.2\,\text{mV}$ at the Coulomb peak indicated by the black dashed line in (a). The green line is a fit to Eq. (3) with $\Gamma_L/2\pi = 1.0\,\text{GHz}$ and $\Gamma_R/2\pi = 40\,\text{GHz}$. (c) Population p as a function of V_{G5} computed using Eq. (5) for $z = 0$. (d) Current variation ΔI as function of the drive power frequency $\omega_e/2\pi$ and V_{G1} at $V_s = 0.2\,\text{mV}$. In each column, the average value of the current was subtracted to highlight the mechanical resonance. Near the Coulomb peak, the nanotube's resonance frequency shows a dip. A small shift in V_{G1} explains the gate voltage difference between the center of the Coulomb peak in (b) and (d). The green line (Lin. fit) is a fit with Eq. (9) and the blue line (Num. int.) is the effective resonance frequency reproduced by numerical integration of the equation of motion (6) with $g_m/2\pi = 0.80\,\text{GHz}$.

using Eq. (3) [Fig. 3(b)], we obtain $\Gamma_L/2\pi = 1.0 \pm 0.1\,\text{GHz}$ and $\Gamma_R/2\pi = 40 \pm 5\,\text{GHz}$. The uncertainty interval in these tunneling rates is determined by fitting the Coulomb peak with two extreme α values given by the uncertainty in α. We then use Eq. (5) to estimate p for any value of μ. The resulting $p(\mu)$ is shown in Fig. 3(c).

We drive the nanotube's motion by a microwave tone at frequency $\omega_e/2\pi$ and drive power $P_0 = -79\,\text{dBm}$ applied to gate G3 [see Fig. 1]. The mechanical resonance causes sharp steps in $I(\omega_e/2\pi)$. Numerically differentiating $I(\omega_e/2\pi)$, the resonance is evident as peaks/dips in $dI/d\omega_e$ [Fig. 3(d)]. The mechanical resonance frequency drops below $\omega_m/2\pi = 294.5\,\text{MHz}$ at values of V_{G1} for which we observed a Coulomb peak [Fig. 3(b)]. We fit this effective resonance frequency, ω_m^{eff}, using Eq. (9). Because $p(\mu)$ is estimated from the tunnel rates and μ_0 is calculated from the lever arm α [Figs. 3(a), 3(b)], the coupling strength g_m is the only fitting parameter. The resistance of the measurement circuit was taken into account by correcting the bias voltage accordingly (see Appendix B 3). We find $g_m/2\pi = 0.80 \pm 0.04\,\text{GHz}$ given the uncertainty over Γ_L and Γ_R. This result leads to a coupling ratio $g_m/\omega_m \simeq 2.72 \pm 0.14$. This ratio is, to the best of our

knowledge, the highest value reported among all other electromechanical platforms. We have estimated $g_m/2\pi$ for other Coulomb peaks in Appendix C.

We have further corroborated $\omega_m^{\text{eff}}(\mu_0)$ by numerically integrating Eq. (6). This approach does not require $p(\mu)$ to be linearized. We estimate $z_{\text{ZPM}} = 0.68\,\text{pm}$ (see Appendix B 4), and considering the values of ω_m, Γ_L and Γ_R extracted from the experiment, we compute $z(t)$ for various sets of values of μ_0, g_m and $z(0)$, choosing $\dot{z}(0) = 0$. We then derive ω_m^{eff} (see Appendix D) and find that $g_m/2\pi \simeq 0.80\,\text{GHz}$ accurately reproduces the dependence of ω_m^{eff} with V_{G1} observed in the experiment [dashed blue line in Fig. 3(d)]. This result is in good agreement with the value of g_m obtained from the fit to Eq. (9). The amplitude of motion, $z(0) \simeq 20 z_{\text{ZPM}} \sim 15\,\text{pm}$, is consistent with the values estimated in previous experiments [45,52]. The value of $z(0)$ only significantly affects the width of the dip in the resonance frequency when $z(0)/z_{\text{ZPM}}$ is larger than Γ_{tot}/g_m, i.e $z(0)/z_{\text{ZPM}} \gtrsim 50$ (see Appendix B 4). We thus confirm that the small displacement limit [Eq. (7)] applies to our experiments.

IV. SEMICLASSICAL ELECTROSTATIC MODEL

We now compare these results with a semiclassical numerical approximation. We calculate the single-particle energy levels of the dot, $\varepsilon_n(z)$, $n = 0, 1, \ldots$. In this case, $\varepsilon_n(z)$ is the contribution to the charging energy, μ, which depends on position z for the gate voltage configuration of the experiment. The occupied energy levels will only impose a constant force on the oscillator. In this case, the value of g_m can be estimated from Eq. (4) as

$$g_m = \frac{z_{\text{ZPM}}}{\hbar} \frac{d\varepsilon_n}{dz}. \tag{10}$$

We compute the levels $\varepsilon_n(z)$ solving explicitly the electric potential field in the plane of motion, $V(z, x)$, using a finite difference method (see Appendix E). Then, the dot energy levels can be obtained from $V(z, x)$ using the Bohr-Sommerfeld equation [57],

$$\oint \sqrt{2m_e(\varepsilon_n(d) - eV(d, x))}\, dx = 2\pi\hbar\left(n + \frac{1}{2}\right). \tag{11}$$

The integral is calculated along a horizontal line at height d from the gates representing the classical path of the electrons. m_e is the electron mass. Figure 4 shows ε for different values of n as a function of the distance d. The values of g_m extracted for different values of d are displayed in Fig. 4 (inset). We find a value $g_m/2\pi \approx 0.80\,\text{GHz}$ for $d = 90\,\text{nm}$, a distance, which is consistent with the geometry of our device (see Appendix E) considering the deformation of the nanotube. The value of g_m decreases slightly with the quantum level index n and as a function of d, setting the range of possibilities for our platform.

V. CONCLUSION

To conclude, we have found that fully suspended carbon nanotube devices can reach ultrastrong coupling $g_m/2\pi \approx 0.80 \pm 0.04\,\text{GHz}$ between single-electron transport and mechanical motion, leading to a coupling ratio of $g_m/\omega_m \simeq$
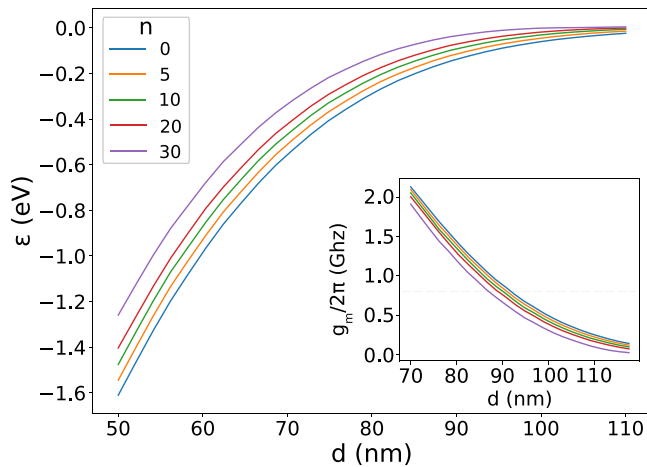
FIG. 4. Energy levels of the quantum dot with $n = 0, 5, 10, 20, 30$ as a function of d obtained from Eq. (11). (Inset) Values of g_m obtained from the dependence of the energy levels with d. The dashed line represent the value $g_m/2\pi = 0.80$ GHz obtained from the experiment.

2.72 ± 0.14, a value that exceeds that obtained with any other electromechanical platform. We have quantified the coupling strength by using rate equations to model the reduction of mechanical resonance frequency observed in our experiments. We separately confirmed the resulting coupling strength with electrostatic simulations based on Bohr-Sommerfeld equations. From these simulations, we extrapolate that this coupling could be enhanced by reducing the distance between the carbon nanotubes and the gates and/or the number of charges in the quantum dot. Using our model to fit measurements from similar suspended carbon nanotube devices ([42] and [41]), we concluded that the ultrastrong coupling regime was present, but went unnoticed. We obtained ratios g_m/ω_m of 1.7 and 1.25, respectively (see Appendix F). This finding suggests that the ultrastrong coupling regime is standard in this type of devices. It allows for an ambitious suite of experiments, ranging from nanomechanical qubits, to information, to work conversion at the nanoscale.

APPENDIX A: SIMPLIFIED ELECTROMECHANICAL MODEL IN THE ADIABATIC REGIME

In this Appendix, we give more details about the electromechanical model presented in Sec. II. We focus here on a single level of the quantum dot, the one inside or closest to the bias window, assuming that there is at most one level inside it [as represented in Fig. 1(b)]. The quantum dot is capacitively coupled to the gates and the effective capacitance depends on the distance between the quantum dot and the gates. Therefore, the vertical motion of the carbon nanotube (CNT) changes the electrochemical potential μ of the quantum dot level. At the first order in z, we have

$$\mu(z) \simeq \mu_0 + \left.\frac{\partial \mu}{\partial z}\right|_{z=0} z, \tag{A1}$$

where $z = 0$ corresponds to the rest position of the carbon nanotube when the quantum dot level is empty. Like for optomechanical systems [8], we define from the above expression the electromechanical coupling strength

$$g_m = \frac{1}{\hbar} \left.\frac{\partial \mu}{\partial z}\right|_{z=0} z_{ZPM}, \tag{A2}$$

and obtain the expression of $\mu(z)$ given by Eq. (4).

So the Hamiltonian describing this simplified model of the electromechanical system is

$$H = \left(\mu_0 + \hbar g_m \frac{\hat{z}}{z_{ZPM}}\right)\hat{n} + \hbar\omega_m \hat{b}^\dagger \hat{b}, \tag{A3}$$

where $\hat{b}$ is the annihilation operator of the considered mechanical mode and $\hat{n}$ the occupation of the quantum dot level. The interaction part of the Hamiltonian therefore writes

$$H_{int} = \hbar g_m \frac{\hat{z}}{z_{ZPM}} \hat{n}, \tag{A4}$$

which corresponds to an electromechanical force

$$\hat{F} = -\frac{dH_{int}}{d\hat{z}} = -\frac{\hbar g_m \hat{n}}{z_{ZPM}} \tag{A5}$$

applied on the resonator.

In addition, electrons tunnel in and out the quantum dot with rates $\gamma_{L/R}^{in}(\mu)$ and $\gamma_{L/R}^{out}(\mu)$ [see Eqs. (1)] and the mechanical resonators undergoes damping at rate γ_m. Our device operates in the semiclassical regime (large phonon number in the resonator) where there is no entanglement between the quantum dot and resonator and no coherences inside the quantum dot. Furthermore, the relevant time scales for the tunneling events $1/\Gamma_{L/R}$ are orders of magnitude shorter than the mechanical dynamics (see Table I). Therefore, we make the adiabatic approximation, namely, we consider that the population $p = \langle \hat{n} \rangle$ of the quantum dot is always the equilibrium one [Eq. (5)], and instantaneously follows the variations of $z = \langle \hat{z} \rangle$. The time evolution of the position of the resonator

TABLE I. Parameters of the case considered in the main text.

Parameter	Name	Value
Bias voltage	V_s	0.2 mV
Left tunneling rate	$\Gamma_L/2\pi$	1.0 ± 0.1 GHz
Right tunneling rate	$\Gamma_R/2\pi$	40 ± 5 GHz
Lifetime broadening	$\Gamma_{tot}/2\pi$	41 ± 5 GHz
Bare mechanical frequency	$\omega_m/2\pi$	294.5 MHz
Zero point motion fluctuation	z_{ZPM}	0.68 ± 0.04 pm
Mechanical quality factor	Q_m	$\leqslant 2000$
Coupling strength	$g_m/2\pi$	0.80 ± 0.04 GHz

is described by the classical equation of motion

$$\ddot{z} + \gamma_m \dot{z} + \omega_m^2 z = \frac{\langle \hat{F} \rangle}{m}, \tag{A6}$$

where m is the mass of the resonator. This equation is consistent with the results from Ref. [43]. In the following, we will consider only a few mechanical periods and thus neglect the mechanical damping due to the high-quality factor $Q_m = \omega_m/\gamma_m$ (see Table I). Using Eq. (A5) and the expression of the zero-point motion fluctuation $z_{ZPM} = \sqrt{\hbar/2m\omega_m}$, we obtain the equation of motion (6).

APPENDIX B: CHARACTERIZATION OF THE EXPERIMENTAL DEVICE

In this Appendix, we describe the suspended carbon nanotube device we used in the experiment and explain how we determined its characteristics.

1. Carbon nanotube device

The suspended carbon nanotube device is similar to the one presented in Refs. [45,51,52]. We fabricated chips from high-resistance Si/SiO_2 substrate by patterning Au/Cr electrodes with E-beam lithography. The carbon nanotubes are grown by CVD on a separate quartz substrate using nanoparticles of Al_2O_3, $Fe(NO_3)$ and $MoO_2(acac)2$ as catalyst and mechanically transferred to the chip. Figure 5 displays a schematic of the device respecting geometric the proportions.

2. Determination of the lever arm α and its uncertainty

The lever arm $\alpha = \frac{|e|C_G^{l\text{dot}}}{C}$ (where $C_G^{l\text{dot}}$ is the capacitance between the gate voltage V_{G1} and the dot, and C the sum of the gate, source C_S and drain capacitances) is critical to the estimation of the coupling strength. The lever arm can be extracted from the two slopes Slope1 and Slope2 of the
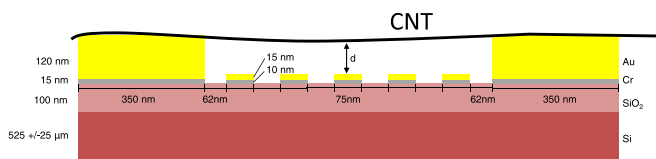

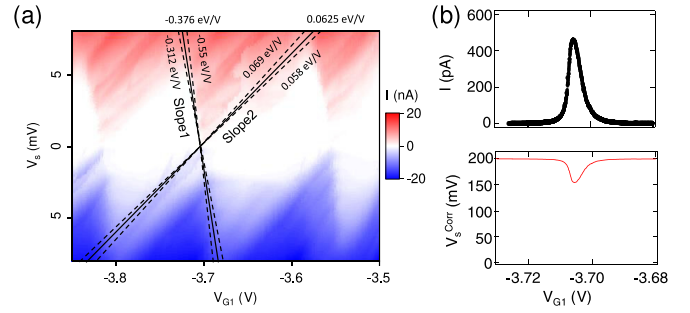FIG. 5. Schematic of the device.

FIG. 6. (a) Coulomb diamonds from Fig. 3(a). The two black lines follow the edge of the diamond and correspond to Slope1 = $-0.376 + 0.064 - 0.174$ eV/V and Slope2 = $0.0625 + 0.0065 - 0.0045$ eV/V. The dashed lines indicate the error in the determination of the slope. (b) Top: Coulomb peak in Fig. 3(b). The measured current I was smoothed. Bottom: Corrected voltage between source and drain contacts as a function of V_{G1}.

Coulomb diamond [Fig. 6(a)] [58]

$$\text{Slope1} = -\frac{|e|C_G^{l\text{dot}}}{C - C_S}, \quad \text{Slope2} = \frac{|e|C_G^{l\text{dot}}}{C_S}. \tag{B1}$$

Combining the two expressions of Eq. (B1), we obtain

$$\alpha = \frac{\text{Slope1} \times \text{Slope2}}{\text{Slope1} - \text{Slope2}} \tag{B2}$$

From Fig. 6(a), we deduce the two slopes Slope1 = $-0.376^{+0.064}_{-0.174}$ eV/V and Slope2 = $0.0625^{+0.0065}_{-0.0045}$ eV/V, resulting in a lever arm:

$$\alpha = 0.054^{+0.007}_{-0.005} \text{ eV/V}. \tag{B3}$$

3. Corrections to the bias voltage

The internal resistance $R_s = 100\text{k}\Omega$ of the IV converter become a significant fraction of the total resistance of the circuit when the device is tuned in a Coulomb peak. It is therefore necessary to introduce a corrected bias voltage,

$$V_s^{\text{Corr}}(V_{G1}) = V_s - I(V_{G1})R_s. \tag{B4}$$

The resulted $V_s^{\text{Corr}}(V_{G1})$ is plotted in Fig. 6(b). The corrected bias voltage was used to fit the Coulomb peak in Fig. 3(b) and the mechanical resonance frequency in Fig. 3(d), which impact the estimation of g_m.

4. Estimation of the carbon nanotube's mass

In the following we estimate the mass m of the CNT and its zero point motion z_{ZPM} from the dependence of the mechanical resonance frequency $\omega_m/2\pi$ with gate voltage [59–61]. We measure the change in current as a function of ω_m [Fig. 7] while sweeping three gate voltages $V_G = \{V_{G1}, V_{G3}, V_{G5}\}$ (V_{G2} and V_{G4} showed leakage currents during the experiment). We observe the increase of ω_m when V_G become more negative until -3.6 V, where the CNT enters the strong bending regime [60,62].

To fit the mechanical frequency, we make use of the continuum model developed in Refs. [60] and [63] to describe the bending modes of a CNT. The displacement z as a function of
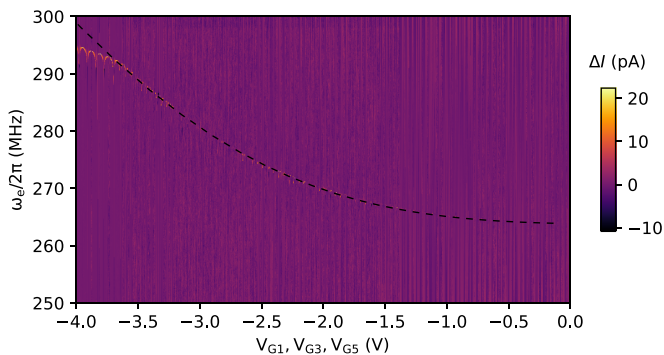
FIG. 7. Mechanical resonance frequency observed for a large sweep of gate voltages $V_G = \{V_{G1}, V_{G3}, V_{G5}\}$ while driving the CNT with a microwave tone at frequency $\omega_e/2\pi$ in a similar manner as Fig. 3(d). The mechanical resonance frequency $\omega_m/2\pi$ is fitted (black dashed line) by self-consistently solving for the eigenmodes of Eq. (B5) together with Eq. (B6) and Eq. (B8). The obtained fitting parameters are $L = 936 \pm 10$ pm, $r = 3.9 \pm 0.2$ pm, $V_0 = 0.82 \pm 0.07$ V, $T_r = 0.7 \pm 0.2$ nN.

time and the position x along the tube axis is modeled by the equation

$$\rho A \frac{\partial^2 z}{\partial t^2} + EI \frac{\partial^4 z}{\partial x^4} - T \frac{\partial^2 z}{\partial x^2} = F(x, t), \quad \text{(B5)}$$

where the first term accounts for the inertia of the CNT, with ρ the mass density of the CNT and A the cross-section area. The second term accounts for the restoring force due to the bending rigidity EI, with E the Young modulus and I the second moment of inertia, while the third term is the restoring force due to the tension T. Finally, the CNT is driven and tuned by the electrostatic force per unit length $F(x, t)$, which is given by [63]

$$F(x, t) = \frac{1}{2} \frac{\partial c_G^l}{\partial z} (V_G(t) - V_0)^2, \quad \text{(B6)}$$

where V_0 is an offset on the dc gate voltage $V_G(t)$ and $c_G^l = C_G/L$, with C_G the total capacitance between the CNT and the gates, is the gate capacitance per unit length. If we approximate the geometry of the problem as that of a cylinder above an infinite plane, then [63]

$$c_G^l(x) = \frac{2\pi \epsilon_0}{\text{arccosh}[(d - z(x))/r]}$$
$$\approx \frac{2\pi \epsilon_0}{\ln(2d/r)} + \frac{2\pi \epsilon_0}{\sqrt{d^2 - r^2} \, \text{arccosh}^2(d/r)} z(x), \quad \text{(B7)}$$

where d is height of the CNT from the gates (at zero gate voltage), r is the radius of the CNT, and the last approximation is valid for $d \gg r, z$. Finally, the tension T on the CNT has two contributions: one due to the pull of CNT towards the gates, which elongates it, and another due to clamping, which can introduce a residual tension T_r and bending (so that the length of the clamped CNT is not the same as the length when unclamped) even when the gate voltage is zero. In conclusion, the tension is given by [63]

$$T = T_r + \frac{EA}{2L} \int_0^L \left(\frac{\partial z}{\partial x} \right)^2 dx. \quad \text{(B8)}$$

TABLE II. Parameters of the estimation of the carbon nanotube's mass and zero-point motion. z_{ZPM}.

Parameter	Estimated value
d	100 nm
L	936 ± 10 nm
r	3.9 ± 0.2 nm
ρ	1350 kg/m^3
E	1.25 TPa
T_r	0.7 ± 0.2 nN
V_0	0.82 ± 0.07 V
C_G	12.9 ± 0.2 aF
$\partial C_G / \partial z$	29.0 ± 0.8 pF/m
m	61 ± 6 ag
z_{ZPM}	0.68 ± 0.04 pm

One can then get frequency of the eigenmodes of (B5) by solving (B5) self-consistently together with (B6) and (B8) (see Ref. [63] for details on these calculations). We use the obtained fundamental frequency to fit the gate voltage dependence measured in Fig. 7. To do the fit, we take $\rho = 1350$ kg/m^3 and $E = 1.25$ TPa, which are standard values for a CNT as it has been widely reported in the literature [63–65]. We further know from the device fabrication that $d \approx 100$ nm. The parameters left to fit are then L, r, T_r, and V_0. The obtained values are shown in Table II and the resulting fit in Fig. 7 (dashed black line). From L and r we further estimate the mass $m = 61 \pm 6$ ag. This gives a zero-point motion $z_{ZPM} = 0.68 \pm 0.04$ pm. It is worth pointing out that the uncertainty on z_{ZPM} does not affect the value of coupling coefficient g_m in the main text, since the expression of the effective mechanical frequency [Eq. (9)] does not depend on z_{ZPM}. Furthermore, we have found that, in the numerical simulations described in the main text, small changes in z_{ZPM} only affect the value found for $z(0)$, which is such that $z(0)/z_{ZPM} \simeq 20$.

5. Estimation of the size of the quantum dot

Here we estimate the length L_{dot} of the quantum dot confinement in the carbon nanotube from the formula of the capacitance between a cylinder and an infinite plane, which for $d \gg z, r$ takes the form

$$C_G^{dot} \approx \frac{2\pi \varepsilon_0 L_{dot}}{\ln(2d/r)} \quad \text{(B9)}$$

where ε_0 is the vacuum permittivity. We reproduce the quantum dot capacitance with respect to V_{G1}, $C_G^{dot} = 1.46$ aF, estimated from the Coulomb diamond in Fig. 3(a), for $L_{dot} = 103$ nm and using the parameters of Table II.

APPENDIX C: FULL SET OF COULOMB PEAKS

We show in Fig. 8 other Coulomb peaks than the one studied in the main text. For each Coulomb peak, there is a dip in the mechanical resonance frequency. We applied the method described in the main text to estimate the coupling strength g_m. The results of each fit are summarized in Table III. Note that in some cases the coupling strength we find exceeds the
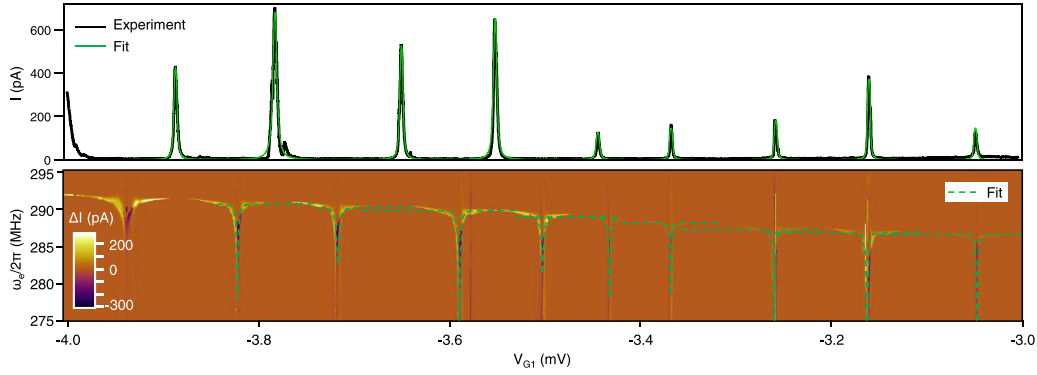
FIG. 8. Top: Fit (green line) of the Coulomb peaks measured under the same condition as in Fig. 3(b) for the extended range of V_{G1} (black line). The center of the Coulomb peaks in gate voltage are shifted from the centers of the frequency dips due to gate voltage drifts. Bottom: Corresponding mechanical resonance frequency obtained by measuring the current variation ΔI. The plot was leveled by column for clarity. The mechanical resonance frequency variations are fitted using the linearization presented in Sec. II, using g_m as fitting parameter. The fitting parameters are displayed in Table III.

one in the main text, but the uncertainty is higher. Our data shows no evidence of a dependence of g_m with gate voltage. However, the range of gate voltage might be too small to reveal a trend.

APPENDIX D: CONFIRMATION OF THE SMALL AMPLITUDE LIMIT

In Sec. II, we did a first-order expansion to obtain the effective mechanical frequency [Eq. (9)] and used this expression to fit the experimental data [Fig. 3(d)] and extract the value of g_m. Here, we go one step further and numerically integrate the equation of motion (6) to confirm the value found for the coupling strength. This numerical integration requires us to choose values for μ_0, g_m and a set of initial conditions ($\dot{z}(0), z(0)$). We choose $\dot{z}(0) = 0$ and therefore $z(0)$ is closely related to the amplitude of the mechanical motion. The other parameters were determined from the experimental data and are given in Table I.

TABLE III. Parameters of the fit of the measurements shown in Fig. 8 from Peak 1 (on the left) to Peak 9 (on the right). The centers of the Coulomb peaks V_{G1}^{pk} are different in gate voltage from the centers of the frequency dips V_{G1}^f due to gate voltage drifts. Note that a few coupling strengths exceed the one of the main text, but the uncertainty is higher.

Param.	$\Gamma_L/2\pi$	$\Gamma_R/2\pi$	V_{G1}^f	V_{G1}^{pk}	$\omega_m/2\pi$	$g_m/2\pi$
Unit	GHz	GHz	V	V	MHz	GHz
Peak 1	0.7	25	-3.821	-3.886	294.6	0.8
Peak 2	1.7	40	-3.716	-3.7815	294.0	0.8
Peak 3	0.9	25	-3.589	-3.6485	293.5	0.9
Peak 4	1.3	30	-3.502	-3.55	292.5	0.7
Peak 5	0.2	30	-3.432	-3.442	292.4	0.8
Peak 6	0.2	20	-3.368	-3.365	291.4	0.8
Peak 7	0.25	20	-3.260	-3.255	290.3	0.8
Peak 8	0.5	15	-3.163	-3.157	289.8	0.8
Peak 9	0.2	20	-3.055	-3.045	289.5	1.0

For each set of values ($\mu_0, g_m, z(0)$), we get $\omega_m^{eff}(\mu_0)$ as the slope of the argument of $z(t) + i\dot{z}(t)/\omega_m$. Figure 9(a) represents $\omega_m^{eff}(\mu_0)$ as a function of the gate voltage for $g_m/2\pi = 0.80$ GHz and different values of $z(0)$. The quantum dot level μ_0 is related to the gate voltage by the relation $\mu_0 = \alpha \Delta V_{G1}$), k and $\alpha = 0.054$ eV/V. This figure shows that
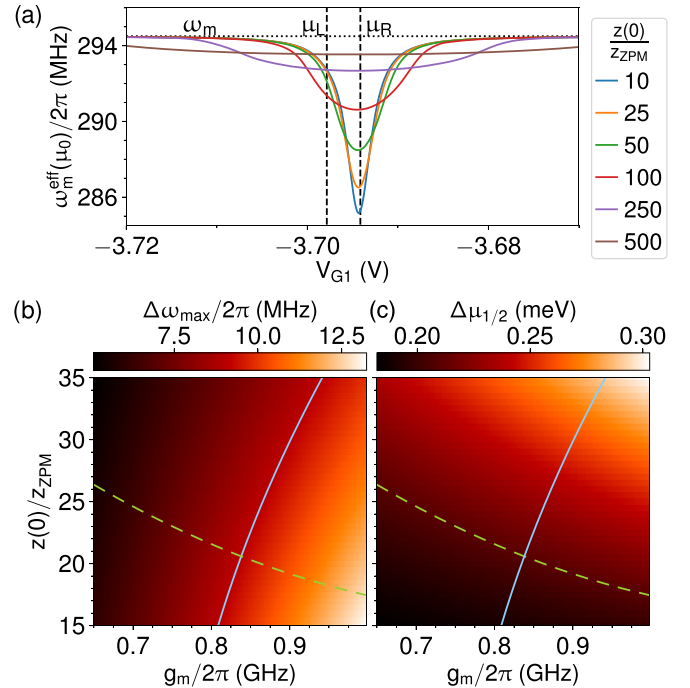
FIG. 9. Characterization of the frequency dip: (a) mechanical resonance frequency as a function of the gate voltage $V_{G5} = V_0 - \mu_0/\alpha$ for $g_m/2\pi = 0.80$ GHz and different values of $z(0)$; (b) depth of the dip $\Delta\omega_{max} = \omega_m - \min_{\mu_0}(\omega_m^{eff}(\mu_0))$ and (c) full width at half-minimum $\Delta\mu_{1/2}$ as a function of the initial position $z(0)$ and the coupling strength g_m. The light blue solid line corresponds to $\Delta\omega_{max}/2\pi = 9.1$ MHz and the dashed green line to $\Delta\mu = 0.21$ meV, which are the characteristics of the experimental plot in Fig. 2(c). The other parameters are given in Table I.

the frequency dip can be characterized by its depth, $\Delta\omega_{\mathrm{max}} = \omega_{\mathrm{m}} - \min_{\mu_0}(\omega_{\mathrm{m}}^{\mathrm{eff}}(\mu_0))$, and full width at half-minimum, $\Delta\mu_{1/2}$. We extract these two parameters from the experimental data: $\Delta\omega_{\mathrm{max}}^{\mathrm{exp}}/2\pi = 9.1\,\mathrm{MHz}$ and $\Delta\mu_{1/2}^{\mathrm{exp}} = 0.21\,\mathrm{meV}$. We then plot maps of $\Delta\omega_{\mathrm{max}}$ and $\Delta\mu_{1/2}$ [Fig. 9(b) and 9(c), respectively] as functions of g_{m} and $z(0)$. The solid light blue line corresponds to the experimental depth and the dashed yellow line to the width at half-minimum. The intersection of the two curves gives us the coupling strength: $g_{\mathrm{m}}/2\pi = 0.84\,\mathrm{GHz}$ for $z(0) = 21z_{\mathrm{ZPM}}$. With this method, we obtain a coupling strength in good agreement with the analytical fit ($g_{\mathrm{m}} = 0.80 \pm 0.04\,\mathrm{GHz}$), thus validating the first-order expansion and, in addition we get an estimate of the amplitude of the mechanical oscillations, $\sim 15\,\mathrm{pm}$.

In Fig. 9(a), we note that the dips are centered on the chemical potential of the right reservoir, μ_{R}. This is because the two barriers have very different tunnel rates: $\Gamma_L \ll \Gamma_R$. In addition, for small amplitudes of the mechanical oscillations, the widths of the dips are very similar, with $\Delta\mu_{1/2} \simeq \hbar\Gamma_{\mathrm{tot}}$. In this limit, the effective frequency is well estimated by Eq. (9). Conversely, the frequency dip becomes larger when the amplitude of the mechanical oscillations makes $\mu(z)$ vary more than $\hbar\Gamma_{\mathrm{tot}}$, that is for $z(0)/z_{\mathrm{ZPM}} > \Gamma_{\mathrm{tot}}/g_{\mathrm{m}}$. In this case, $\mu(z)$ can enter the bias window even for a μ_0 relatively far outside. Note that $\hbar\Gamma_{\mathrm{tot}}$ is the length of the interval centered in μ_{R} over which $p(\mu)$ varies significantly, see Eqs. (2) and (5). For the experimental device, we have $\Gamma_{\mathrm{tot}}/g_{\mathrm{m}} = 50$ so we can reasonably use the small amplitude limit.

APPENDIX E: ELECTRIC FIELD AND SINGLE-PARTICLE ENERGY LEVELS

We used a finite-differences method in order to calculate the electric potential field in a vertical plane on the device. In this calculation we considered a 1200×1200 grid in order to obtain enough resolution, and imposed the five gates in the bottom on the figure and the two lateral electrodes. The top boundary of the device is considered at sufficient height from the device and kept at constant zero voltage, obtaining a negligible impact on the system [66,67].

Equation (11) requires a path integral along the classical electrons trajectory. In Fig. 10, we sketch this situation. The electrons path representing the nanotube is considered as a straight horizontal line at a certain distance from the gates, moving from left lead to right.

APPENDIX F: ESTIMATION OF THE COUPLING STRENGTH FOR SIMILAR DEVICES IN THE LITERATURE

We apply our model to fit measurements obtained with similar devices [41,42] and show that devices in these studies are also in the ultrastrong coupling regime. First we fit the results of Huttel *et al.* [41] in Fig. 11(a). We find $g_{\mathrm{m}}/2\pi \approx 0.5\,\mathrm{GHz}$. The other parameters of the fit are $\Gamma_{\mathrm{L}} = 55\,\mathrm{GHz}$, $\Gamma_{\mathrm{R}} = 10\,\mathrm{GHz}$ and $\omega_{\mathrm{m}}/2\pi = 296.5\,\mathrm{MHz}$, considering $V_{\mathrm{s}} = 0.1\,\mathrm{mV}$ from the paper and $\alpha = 0.1$. The lever α is not mentioned so we explored a range of value from $\alpha = 0.05$ to $\alpha = 0.2$. The best fit is obtained with $\alpha = 0.1$. We also
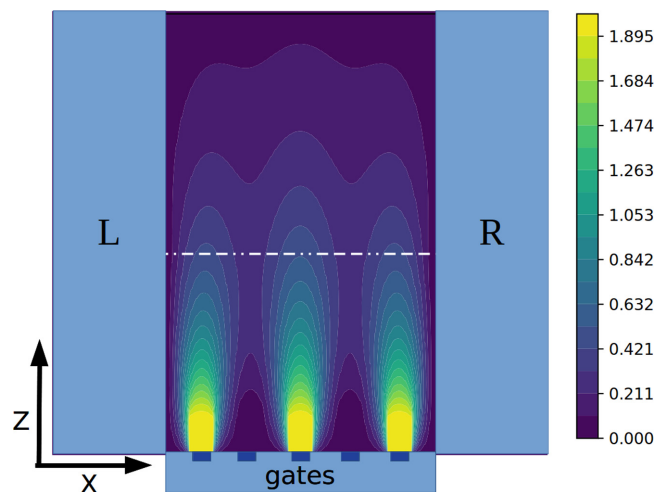
FIG. 10. Electrical voltage in the vertical plane of the device in an arbitrary gates configuration. The nanotube is represented with an horizontal white line between the electrodes L and R, at a certain distance from the gates. This line represents the integration path of Eq. (11) of the main text.

fitted the result published by Meerwaldt *et al.* [42] that display all the parameters our model requires, see Fig. 11(b). We find a coupling of $g_{\mathrm{m}}/2\pi = 0.36\,\mathrm{GHz}$ for $\Gamma_{\mathrm{L}}/2\pi = 127\,\mathrm{GHz}$, $\Gamma_{\mathrm{R}}/2\pi = 30\,\mathrm{GHz}$ and $\omega_{\mathrm{m}}/2\pi = 286.88\,\mathrm{MHz}$. In conclusion we find a coupling strength of $g_{\mathrm{m}}/2\pi \approx 0.5\,\mathrm{GHz}$ and $\Gamma_{\mathrm{R}}/2\pi = 30\,\mathrm{GHz}$ in these two devices giving a $g_{\mathrm{m}}/\omega_{\mathrm{m}}$ ratio of 1.7 and 1.25, respectively.
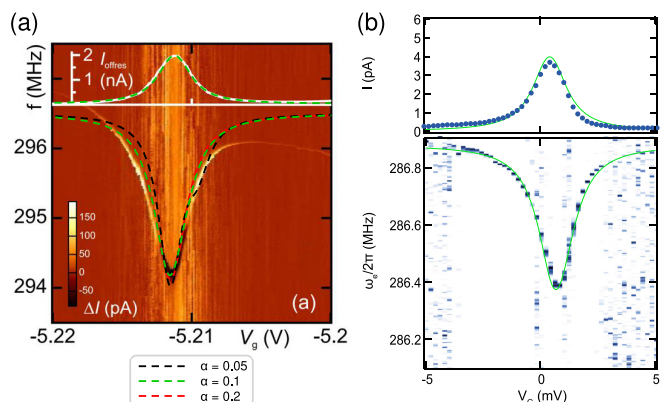
FIG. 11. Fits of the Coulomb peak (top plots) and mechanical resonance frequency (bottom plots) for experimental results from other groups using our model. (a) Results reproduced from Fig. 4 of Ref. [41]. The three curves correspond to different values of the lever arm: $\alpha = 0.05$ ($\Gamma_{\mathrm{L}}/2\pi = 20\,\mathrm{GHz}$, $\Gamma_{\mathrm{R}}/2\pi = 5\,\mathrm{GHz}$, $g_{\mathrm{m}}/2\pi = 0.34\,\mathrm{GHz}$), $\alpha = 0.1$ ($\Gamma_{\mathrm{L}}/2\pi = 55\,\mathrm{GHz}$, $\Gamma_{\mathrm{R}}/2\pi = 10\,\mathrm{GHz}$, $g_{\mathrm{m}}/2\pi = 0.5\,\mathrm{GHz}$) and $\alpha = 0.2$ ($\Gamma_{\mathrm{L}}/2\pi = 110\,\mathrm{GHz}$, $\Gamma_{\mathrm{R}}/2\pi = 19\,\mathrm{GHz}$, $g_{\mathrm{m}}/2\pi = 0.7\,\mathrm{GHz}$). (b) Results reproduced from Fig. 4 of Ref. [42]. The parameters of the fit were $\Gamma_{\mathrm{L}}/2\pi = 127\,\mathrm{GHz}$, $\Gamma_{\mathrm{R}}/2\pi = 30\,\mathrm{GHz}$, $g_{\mathrm{m}}/2\pi = 0.36\,\mathrm{MHz}$. The mechanical resonance frequency $\omega_{\mathrm{m}}/2\pi = 286.88\,\mathrm{MHz}$ and the lever arm $\alpha = 0.38$ are given in the paper. The Coulomb peak is shifted by 0.8 mV between the top and bottom panel.

[1] M. LaHaye, J. Suh, P. Echternach, K. C. Schwab, and M. L. Roukes, Nanomechanical measurements of a superconducting qubit, Nature (London) **459**, 960 (2009).

[2] J. Moser, J. Güttinger, A. Eichler, M. J. Esplandiu, D. Liu, M. Dykman, and A. Bachtold, Ultrasensitive force detection with a nanotube mechanical resonator, Nature Nanotechnol. **8**, 493 (2013).

[3] Y. Wang, G. Micchi, and F. Pistolesi, Sensitivity of the mixing-current technique for the detection of mechanical motion in the coherent tunnelling regime, J. Phys.: Condens. Matter **29**, 465304 (2017).

[4] S. L. de Bonis, C. Urgell, W. Yang, C. Samanta, A. Noury, J. Vergara-Cruz, Q. Dong, Y. Jin, and A. Bachtold, Ultrasensitive displacement noise measurement of carbon nanotube mechanical resonators, Nano Lett. **18**, 5324 (2018).

[5] A. D. O'Connell, M. Hofheinz, M. Ansmann, R. C. Bialczak, M. Lenander, E. Lucero, M. Neeley, D. Sank, H. Wang, M. Weides, J. Wenner, J. M. Martinis, and A. N. Cleland, Quantum ground state and single-phonon control of a mechanical resonator, Nature (London) **464**, 697 (2010).

[6] T. Palomaki, J. Teufel, R. Simmonds, and K. W. Lehnert, Entangling mechanical motion with microwave fields, Science **342**, 710 (2013).

[7] A. Reed, K. Mayer, J. Teufel, L. Burkhart, W. Pfaff, M. Reagor, L. Sletten, X. Ma, R. Schoelkopf, E. Knill, and K. W. Lehnert, Faithful conversion of propagating quantum information to mechanical motion, Nature Phys. **13**, 1163 (2017).

[8] M. Aspelmeyer, T. J. Kippenberg, and F. Marquardt, Cavity optomechanics, Rev. Mod. Phys. **86**, 1391 (2014).

[9] C. Elouard, M. Richard, and A. Auffèves, Reversible work extraction in a hybrid opto-mechanical system, New J. Phys. **17**, 055018 (2015).

[10] J. Monsel, C. Elouard, and A. Auffèves, An autonomous quantum machine to measure the thermodynamic arrow of time, npj Quantum Inf. **4**, 59 (2018).

[11] C. W. Wächtler, P. Strasberg, and G. Schaller, Proposal of a Realistic Stochastic Rotor Engine Based on Electron Shuttling, Phys. Rev. Appl. **12**, 024001 (2019).

[12] C. W. Wächtler, P. Strasberg, S. H. L. Klapp, G. Schaller, and C. Jarzynski, Stochastic thermodynamics of self-oscillations: The electron shuttle, New J. Phys. **21**, 073009 (2019).

[13] A. Bachtold, J. Moser, and M. Dykman, Mesoscopic physics of nanomechanical systems, arXiv:2202.01819.

[14] K. Hammerer, M. Wallquist, C. Genes, M. Ludwig, F. Marquardt, P. Treutlein, P. Zoller, J. Ye, and H. J. Kimble, Strong Coupling of a Mechanical Oscillator and a Single Atom, Phys. Rev. Lett. **103**, 063005 (2009).

[15] S. D. Bennett, L. Cockins, Y. Miyahara, P. Grütter, and A. A. Clerk, Strong Electromechanical Coupling of an Atomic Force Microscope Cantilever to a Quantum Dot, Phys. Rev. Lett. **104**, 017203 (2010).

[16] D. Hunger, S. Camerer, T. W. Hänsch, D. König, J. P. Kotthaus, J. Reichel, and P. Treutlein, Resonant Coupling of a Bose-Einstein Condensate to a Micromechanical Oscillator, Phys. Rev. Lett. **104**, 143002 (2010).

[17] P. Rabl, P. Cappellaro, M. G. Dutt, L. Jiang, J. Maze, and M. D. Lukin, Strong magnetic coupling between an electronic spin qubit and a mechanical resonator, Phys. Rev. B **79**, 041302(R) (2009).

[18] S. Kolkowitz, A. C. B. Jayich, Q. P. Unterreithmeier, S. D. Bennett, P. Rabl, J. Harris, and M. D. Lukin, Coherent sensing of a mechanical resonator with a single-spin qubit, Science **335**, 1603 (2012).

[19] B. H. Schneider, S. Etaki, H. S. J. van der Zant, and G. A. Steele, Coupling carbon nanotube mechanics to a superconducting circuit, Sci. Rep. **2**, 599 (2012).

[20] P. Treutlein, C. Genes, K. Hammerer, M. Poggio, and P. Rabl, Hybrid mechanical systems, in *Cavity Optomechanics* (Springer, Berlin, 2014), pp. 327–351.

[21] J.-M. Pirkkalainen, S. Cho, F. Massel, J. Tuorila, T. Heikkilä, P. Hakonen, and M. Sillanpää, Cavity optomechanics mediated by a quantum two-level system, Nature Commun. **6**, 6981 (2015).

[22] G. A. Steele, A. K. Hüttel, B. Witkamp, M. Poot, H. B. Meerwaldt, L. P. Kouwenhoven, and H. S. van der Zant, Strong coupling between single-electron tunneling and nanomechanical motion, Science **325**, 1103 (2009).

[23] B. Lassagne, Y. Tarakanov, J. Kinaret, D. Garcia-Sanchez, and A. Bachtold, Coupling Mechanics to Charge Transport in Carbon Nanotube Mechanical Resonators, Science **325**, 1107 (2009).

[24] J.-M. Pirkkalainen, S. U. Cho, J. Li, G. S. Paraoanu, P. J. Hakonen, and M. A. Sillanpää, Hybrid circuit cavity quantum electrodynamics with a micromechanical resonator, Nature (London) **494**, 211 (2013).

[25] O. Arcizet, V. Jacques, A. Siria, P. Poncharal, P. Vincent, and S. Seidelin, A Single Nitrogen-Vacancy Defect Coupled to a Nanomechanical Oscillator, Nature Phys. **7**, 879 (2011).

[26] I. Yeo, P.-L. de Assis, A. Gloppe, E. Dupont-Ferrier, P. Verlot, N. S. Malik, E. Dupuy, J. Claudon, J.-M. Gérard, A. Auffèves, G. Nogues, S. Seidelin, J.-P. Poizat, O. Arcizet, and M. Richard, Strain-mediated coupling in a quantum dot–mechanical oscillator hybrid system, Nature Nanotechnol. **9**, 106 (2014).

[27] J. Kettler, N. Vaish, L. M. de Lépinay, B. Besga, P.-L. de Assis, O. Bourgeois, A. Auffèves, M. Richard, J. Claudon, J.-M. Gérard, B. Pigeau, O. Arcizet, P. Verlot, and J.-P. Poizat, Inducing micromechanical motion by optical excitation of a single quantum dot, Nature Nanotechnol. **16**, 283 (2021).

[28] P. D. Nation, J. Suh, and M. P. Blencowe, Ultrastrong optomechanics incorporating the dynamical Casimir effect, Phys. Rev. A **93**, 022510 (2016).

[29] O. Shevchuk, G. A. Steele, and Y. M. Blanter, Strong and tunable couplings in flux-mediated optomechanics, Phys. Rev. B **96**, 014508 (2017).

[30] K. E. Khosla, M. R. Vanner, N. Ares, and E. A. Laird, Displacemon Electromechanics: How to Detect Quantum Interference in a Nanomechanical Resonator, Phys. Rev. X **8**, 021052 (2018).

[31] M. Kounalakis, Y. M. Blanter, and G. A. Steele, Flux-mediated optomechanics with a transmon qubit in the single-photon ultrastrong-coupling regime, Phys. Rev. Res. **2**, 023335 (2020).

[32] L. Neumeier and D. E. Chang, Exploring unresolved sideband, optomechanical strong coupling using a single atom coupled to a cavity, New J. Phys. **20**, 083004 (2018).

[33] L. Neumeier, T. E. Northup, and D. E. Chang, Reaching the optomechanical strong-coupling regime with a single atom in a cavity, Phys. Rev. A **97**, 063857 (2018).

[34] T. T. Heikkilä, F. Massel, J. Tuorila, R. Khan, and M. A. Sillanpää, Enhancing Optomechanical Coupling

via the Josephson Effect, Phys. Rev. Lett. **112**, 203603 (2014).

[35] A. Rimberg, M. Blencowe, A. Armour, and P. Nation, A cavity-Cooper pair transistor scheme for investigating quantum optomechanics in the ultra-strong coupling regime, New J. Phys. **16**, 055008 (2014).

[36] J. Manninen, M. T. Haque, D. Vitali, and P. Hakonen, Enhancement of the optomechanical coupling and Kerr nonlinearity using the Josephson capacitance of a Cooper-pair box, Phys. Rev. B **105**, 144508 (2022).

[37] A. Benyamini, A. Hamo, S. V. Kusminskiy, F. von Oppen, and S. Ilani, Real-space tailoring of the electron–phonon coupling in ultraclean nanotube mechanical resonators, Nature Phys. **10**, 151 (2014).

[38] J. Moser, A. Eichler, J. Güttinger, M. I. Dykman, and A. Bachtold, Nanotube mechanical resonators with quality factors of up to 5 million, Nature Nanotechnol. **9**, 1007 (2014).

[39] E. A. Laird, F. Pei, W. Tang, G. A. Steele, and L. P. Kouwenhoven, A high quality factor carbon nanotube mechanical resonator at 39 GHz, Nano Lett. **12**, 193 (2012).

[40] M. T. Woodside and P. L. McEuen, Scanned probe imaging of single-electron charge states in nanotube quantum dots, Science **296**, 1098 (2002).

[41] A. K. Hüttel, H. B. Meerwaldt, G. A. Steele, M. Poot, B. Witkamp, L. P. Kouwenhoven, and H. S. J. van der Zant, Single electron tunnelling through high-Q single-wall carbon nanotube NEMS resonators, Phys. Status Solidi B **247**, 2974 (2010).

[42] H. B. Meerwaldt, G. Labadze, B. H. Schneider, A. Taspinar, Y. M. Blanter, H. S. J. van der Zant, and G. A. Steele, Probing the charge of a quantum dot with a nanomechanical resonator, Phys. Rev. B **86**, 115454 (2012).

[43] G. Micchi, R. Avriller, and F. Pistolesi, Mechanical Signatures of the Current Blockade Instability in Suspended Carbon Nanotubes, Phys. Rev. Lett. **115**, 206802 (2015).

[44] G. Micchi, R. Avriller, and F. Pistolesi, Electromechanical transition in quantum dots, Phys. Rev. B **94**, 125417 (2016).

[45] Y. Wen, N. Ares, F. J. Schupp, T. Pei, G. A. D. Briggs, and E. A. Laird, A coherent nanomechanical oscillator driven by single-electron tunnelling, Nature Phys. **16**, 75 (2020).

[46] C. Urgell, W. Yang, S. De Bonis, C. Samanta, M. J. Esplandiu, Q. Dong, Y. Jin, and A. Bachtold, Cooling and self-oscillation in a nanotube electromechanical resonator, Nature Phys. **16**, 32 (2020).

[47] I. Khivrich, A. A. Clerk, and S. Ilani, Nanomechanical pump–probe measurements of insulating electronic states in a carbon nanotube, Nature Nanotechnol. **14**, 161 (2019).

[48] F. Pistolesi, A. N. Cleland, and A. Bachtold, Proposal for a Nanomechanical Qubit, Phys. Rev. X **11**, 031027 (2021).

[49] P. Forn-Díaz, L. Lamata, E. Rico, J. Kono, and E. Solano, Ultrastrong coupling regimes of light-matter interaction, Rev. Mod. Phys. **91**, 025005 (2019).

[50] F. Valmorra, K. Yoshida, L. C. Contamin, S. Messelot, S. Massabeau, M. R. Delbecq, M. C. Dartiailh, M. M. Desjardins, T. Cubaynes, Z. Leghtas, K. Hirakawa, J. Tignon, S. Dhillon, S. Balibar, J. Mangeney, A. Cottet, and T. Kontos, Vacuum-field-induced THz transport gap in a carbon nanotube quantum dot, Nature Commun. **12**, 5490 (2021).

[51] N. Ares, T. Pei, A. Mavalankar, M. Mergenthaler, J. H. Warner, G. A. D. Briggs, and E. A. Laird, Resonant Optomechanics with a Vibrating Carbon Nanotube and a Radio-Frequency Cavity, Phys. Rev. Lett. **117**, 170801 (2016).

[52] Y. Wen, N. Ares, T. Pei, G. Briggs, and E. A. Laird, Measuring carbon nanotube vibrations using a single-electron transistor as a fast linear amplifier, Appl. Phys. Lett. **113**, 153101 (2018).

[53] C. W. J. Beenakker, Theory of coulomb-blockade oscillations in the conductance of a quantum dot, Phys. Rev. B **44**, 1646 (1991).

[54] J. Koch, F. von Oppen, and A. V. Andreev, Theory of the Franck-Condon blockade regime, Phys. Rev. B **74**, 205438 (2006).

[55] R. Leturcq, C. Stampfer, K. Inderbitzin, L. Durrer, C. Hierold, E. Mariani, M. G. Schultz, F. Von Oppen, and K. Ensslin, Franck–condon blockade in suspended carbon nanotube quantum dots, Nature Phys. **5**, 327 (2009).

[56] E. Mariani and F. von Oppen, Electron-vibron coupling in suspended carbon nanotube quantum dots, Phys. Rev. B **80**, 155411 (2009).

[57] Y. V. Nazarov and Y. M. Blanter, *Quantum Transport: Introduction to Nanoscience* (Cambridge University Press, Cambridge, 2009).

[58] R. Hanson, L. P. Kouwenhoven, J. R. Petta, S. Tarucha, and L. M. K. Vandersypen, Spins in few-electron quantum dots, Rev. Mod. Phys. **79**, 1217 (2007).

[59] V. Sazonova, Y. Yaish, H. Üstünel, D. Roundy, T. A. Arias, and P. L. McEuen, A tunable carbon nanotube electromechanical oscillator, Nature (London) **431**, 284 (2004).

[60] M. Poot, B. Witkamp, M. A. Otte, and H. S. J. van der Zant, Modelling suspended carbon nanotube resonators, Phys. Status Solidi B **244**, 4252 (2007).

[61] C. C. Wu and Z. Zhong, Capacitive spring softening in single-walled carbon nanotube nanoelectromechanical resonators, Nano Lett. **11**, 1448 (2011).

[62] S. Sapmaz, Y. M. Blanter, L. Gurevich, and H. S. J. van der Zant, Carbon nanotubes as nanoelectromechanical systems, Phys. Rev. B **67**, 235414 (2003).

[63] B. Witkamp, High-frequency nanotube resonators, Ph.D. thesis, Technische Universiteit Delft, 2009.

[64] H. B. Meerwaldt, G. A. Steele, and H. S. J. van der Zant, Carbon nanotubes: nonlinear highQ resonators with strong coupling to single-electron tunneling, in *Fluctuating Nonlinear Oscillators: From Nanomechanics to Quantum Superconducting Circuits* (Oxford University Press, Oxford, 2012).

[65] A. Castellanos-Gomez, H. B. Meerwaldt, W. J. Venstra, H. S. J. van der Zant, and G. A. Steele, Strong and tunable mode coupling in carbon nanotube resonators, Phys. Rev. B **86**, 041402(R) (2012).

[66] S. Heinze, M. Radosavljević, J. Tersoff, and P. Avouris, Unexpected scaling of the performance of carbon nanotube schottky-barrier transistors, Phys. Rev. B **68**, 235418 (2003).

[67] S. Heinze, J. Tersoff, R. Martel, V. Derycke, J. Appenzeller, and P. Avouris, Carbon Nanotubes as Schottky Barrier Transistors, Phys. Rev. Lett. **89**, 106801 (2002).